HAL
open science

Simulation Analysis and Experimental Evaluation of the Transient Behavior of a Reluctance Magnetic Coupling

Thierry Lubin, Alexandre Colle

To cite this version:

Thierry Lubin, Alexandre Colle. Simulation Analysis and Experimental Evaluation of the Transient Behavior of a Reluctance Magnetic Coupling. IET Electric Power Applications, 2020, 10.1049/iet-epa.2019.0678 . hal-02446524

HAL Id: hal-02446524

https://hal.science/hal-02446524v1

Submitted on 20 Jan 2020

HAL is a multi-disciplinary open access archive for the deposit and dissemination of scientific research documents, whether they are published or not. The documents may come from teaching and research institutions in France or abroad, or from public or private research centers.

L'archive ouverte pluridisciplinaire **HAL**, est destinée au dépôt et à la diffusion de documents scientifiques de niveau recherche, publiés ou non, émanant des établissements d'enseignement et de recherche français ou étrangers, des laboratoires publics ou privés.

Simulation Analysis and Experimental Evaluation of the Transient Behavior of a Reluctance Magnetic Coupling

Thierry LUBIN [1*], Alexandre COLLE [1]

[1] Groupe de Recherche en Énergie Electrique de Nancy (GREEN), Faculté des Sciences et Technologies
Université de Lorraine, 54506 Vandœuvre-lès-Nancy, France.
[*]Thierry.lubin@univ-lorraine.fr

Abstract: The aim of this paper is to present the dynamic behavior of two co-axial rotating shafts connected by a reluctance magnetic coupling. The analysis is based on nonlinear differential equations of motion. The reluctance magnetic coupling is modeled by an equivalent torsional stiffness coefficient and an additional viscous damping coefficient to account for the effects of induced currents in the salient-pole during the transient. These coefficients are obtained from 3D finite element electromagnetic models. In order to evaluate the accuracy of the proposed model, several transient responses for the shaft line are considered. The simulation results are compared with those obtained from measurements.

1. Introduction

Magnetic couplings are generally used to transmit a rotational movement between two shafts through a sealed wall in order to avoid any contact with the product to be treated. The torque transmission between the two shafts is carried out without contact by the interaction between magnetic fields in the air-gap. There are two main types of magnetic couplings: synchronous and asynchronous (eddy-current), with radial and axial flux topologies. The synchronous magnetic coupling [1-5] consists of rare-earth permanent magnets (PMs) placed on both rotors that move at the same speed. It has a pull-out torque, which is the maximum torque that can be transmitted by the coupling before the stall. For eddy-current couplings [6-9], one of the two rotors is made with a conductive plate, usually copper. The torque transmission is due to the induced currents which depend on the relative speed between the two rotors (slip). This results in Joule losses, and adequate cooling may be necessary to avoid overheating.

Among classical magnetic couplings technologies, reluctance torque magnetic couplings have received very little attention in the literature [10, 11]. Yet, it can be a good option when one of the mechanical shafts has to be placed in high temperature environment where permanent magnets cannot be used [11]. The goal of this paper is to develop a transient model for a reluctance magnetic coupling placed between two shafts. It is part of the author's works on the dynamic performance of magnetic couplings, following those recently performed on two-face permanent magnets and eddy-current couplings [12-14].

While the steady-state performance of magnetic couplings is widely studied in the literature, it should be noted that very little attention is paid to their transient behavior. However, this can be of great importance if a magnetic coupling is used to transmit the torque between two shafts for servomechanism. Previous published papers only concern classical magnetic couplings topologies or magnetic gear [12-14], [17-21]. To the best knowledge of the authors, no studies have been conducted to analyze the transient behavior of a reluctance magnetic coupling.

For synchronous magnetic couplings or magnetic gears with permanent magnets placed on both rotors [12], [17, 18], it has been shown that a stiffness coefficient is sufficient in the transient model to correctly predict the speed response during start-up. Indeed, the impact of induced currents in the magnets during the transient can be neglected due to the low value of their electrical conductivity. An important experimental result given in [12] shows that the synchronism can be lost for an abrupt start-up of the motor which cause the load to stall. This will be no longer the case for a reluctance magnetic coupling due to the supplementary torque caused by induced currents in the salient-pole during the transient, as shown later in the paper.

For eddy-current magnetic couplings, the dynamic behavior is well predicted by considering only the damping coefficient in the transient model [19-21]. It is shown that no oscillation appears on the speed response during start-up [13], as is the case for synchronous magnetic couplings with permanent magnets on both sides [12]. A comparison of the transient performances between eddy-current coupling and PMs synchronous coupling is given in [14].

For the reluctance magnetic coupling studied in this paper, the analysis is more complicated in terms of modeling because of the induced currents in the salient-pole during the transients that cannot be overlooked to correctly predict the dynamic performances. To obtain good prediction for the dynamic behavior, it will be shown in the next parts that it is necessary to take into account both stiffness and damping coefficients in the transient model.

The paper is organized as follows. The description of the studied reluctance magnetic coupling is presented in section 2. In section 3, the torsional spring stiffness and the viscous damping coefficients representing the reluctance magnetic coupling will be determined by using 3-D finite element simulations. Based on the knowledge of these coefficients, a mathematical model for the dynamic behavior of the shaft line will be developed in section 4 and used to study several transient regimes such as starting. It will be shown in section 5 that the synchronization between the two shafts can be lost in the event of a sudden start if the air-gap is too large. The positive impact of induced currents in the salient-pole for the stability will also be demonstrated.

The simulation results will be compared to experimental tests to demonstrate the accuracy of the proposed mathematical model

2. Description of the Axial-Field Reluctance Magnetic Coupling

As shown in Fig. 1, an axial-field reluctance magnetic coupling is composed of two discs facing each other and separated by a small air-gap. One disc is made with permanent magnets (PMs) regularly distributed along the circumferential direction in order to obtain north and south poles. The second disc consists of ferromagnetic salient poles, their number being the same as PMs. If one of the rotors is rotated, there is a change in energy stored in the magnetic circuit. This change is resisted by a restoring torque toward the aligned position. The angular shift between the two discs is directly related to the transmitted torque value. In steady state, the two rotors rotate in synchronism.

The geometrical parameters of the studied reluctance magnetic coupling are given in Fig. 1 and defined in Table 1. The prototype, which is placed between two electric motors, is shown in Fig. 2. The parameters given in Table 1 have been obtained after an optimization procedure but this is not within the scope of this paper. The optimization goals were to obtain a pull-out torque of 15 Nm for an air-gap length of 3 mm for a external radius set at R_2 = 60 mm and the minimum volume for the magnets.

3. 3-D Finite Element Modelling

The first step before studying the dynamic behavior of the shaft line is to determine the mechanical parameters that represent the magnetic coupling as well as possible. The mechanical model of the system is shown in Fig. 3. It is composed of a load connected to a motor (drive torque) via the reluctance coupler and is equivalent to the test bench shown in Fig. 2 where J_1 and B_1 are the moment of inertia and the friction coefficient of the drive rotor, respectively; J_2 and B_2 denote the moment of inertia and the friction coefficient of the load, respectively. T_1 is the drive torque (dc motor), and T_2 is the load torque (dc generator).

As shown in Fig. 3, the reluctance magnetic coupling can be seen as a rotary spring with torsional stiffness K and a viscous rotary damper with a damping factor B connected in parallel. The spring stiffness is directly related to the synchronous torque between the magnets and the salient pole. The damping effect is due to the eddy current loss in the salient-pole that only exists during the transient.

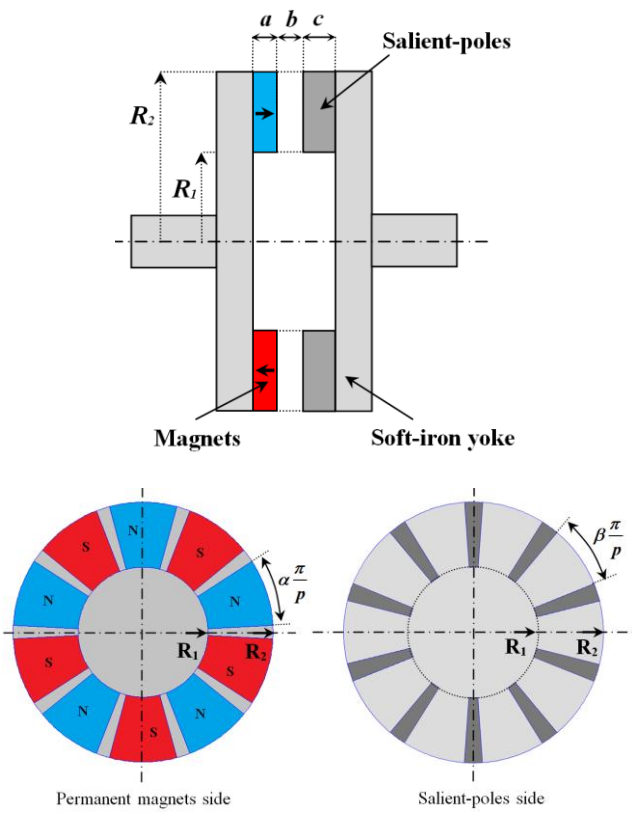

Fig. 1. Geometry of the studied reluctance magnetic coupling

Table 1: Geometrical parameters of the magnetic coupling

Symbol	Quantity	value
R_1	Inner radius of the magnets	30 mm
R_2	Outer radius of the magnets	60 mm
a	Magnets thickness	10 mm
b	Air-gap length	variable
c	Salient-pole thickness	15 mm
α	PMs pole-arc to pole-pitch ratio	0.83
β	Slot-opening to pole-pitch ratio	0.77
p	Pole-pairs number	5
B_r	Remanence of the magnets	1.25 T
σ	Conductivity of the salient-pole	6 MS/m

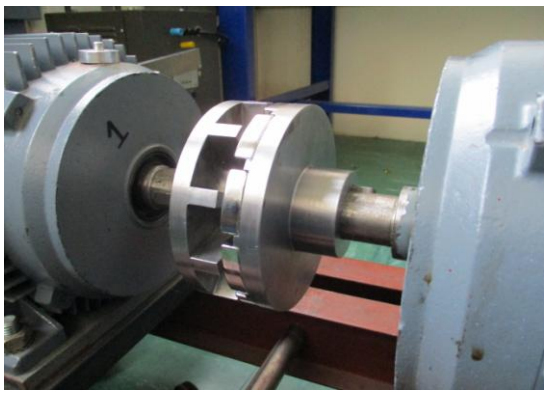

Fig. 2. Reluctance magnetic coupling prototype placed on the test bench between two electrical machines

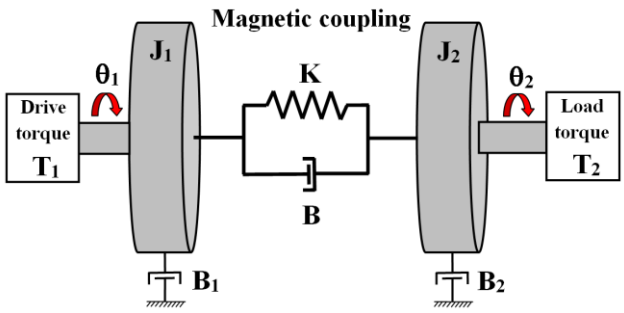

Fig. 3. Equivalent mechanical system of the shaft line with the magnetic coupling

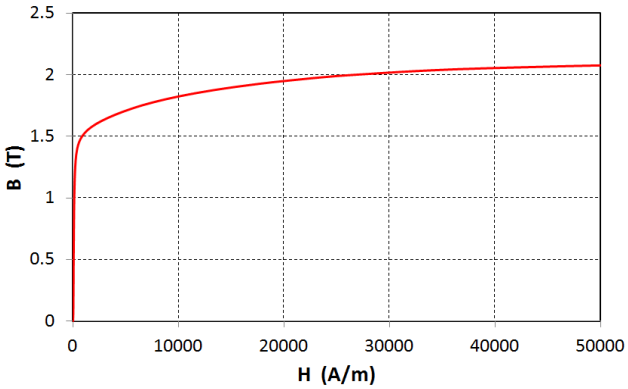

Fig. 4. *B-H curve of the salient poles used in 3D FEM*

Therefore, the torque transmitted through the magnetic coupling can be written as the sum of two terms

$$T_c = K(\theta_1 - \theta_2) + B(\Omega_1 - \Omega_2) \qquad (1)$$

where θ_1 and θ_2 are the drive and the load rotor position, respectively, and $\Omega_1 = d\theta_1/dt$, $\Omega_2 = d\theta_2/dt$ represent the speeds of each of the rotors. In steady state, the two rotors rotate in synchronism ($\Omega_1 = \Omega_2$) and the transmitted torque only depends on the load angle defined as $\delta = \theta_1 - \theta_2$.

Here, we have assumed that the spring torque is directly proportional to the relative position of its two ends, as well as for the damper torque but for the relative angular speed. We will see in the next section that the reluctance torque coupler has a non-linear behavior and the associate characteristics should be linearised to define the coefficients K and B in (1).

Three dimensional finite element simulations (3-D FEM) are performed using COMSOL Multiphysics® to define K and B. The geometrical parameters given in Table 1 and the actual geometry of the coupling (Fig. 1) are considered for the simulations. The non-linear magnetic property of the iron parts (B-H curve) has been taken into account, Fig. 4.

In order to show the effect of the air-gap length, three values for the air-gap were considered (b = 3 mm, b = 5 mm, and b = 7mm). For the determination of the torsional stiffness coefficient, a 3-D magnetostatic formulation was used while a fully 3-D transient electromagnetic model was required to obtain the viscous damping coefficient. In each case, the mesh size was refined until converging results were obtained [15]-[16].

3.1. Torsional Stiffness Coefficient

The torque as a function of the load angle δ is shown in Fig. 5. The results have been obtained for three values of the air-gap length. As can be seen, the torque varies almost sinusoidally with the load angle δ with a period equal to π/p and a peak value T_{max} that corresponds to the pull-out torque. This is a classical result for reluctance-type actuators [10].

Of course, the pull-out torque decreases as the air-gap length increases. From Fig. 5, the reluctance torque can be approximated by a sinusoidal function as follows

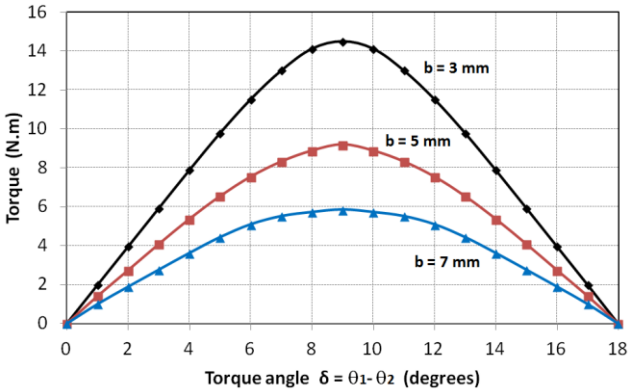

Fig. 5. *Reluctance torque as a function of the load angle for 3 values of the air-gap length*

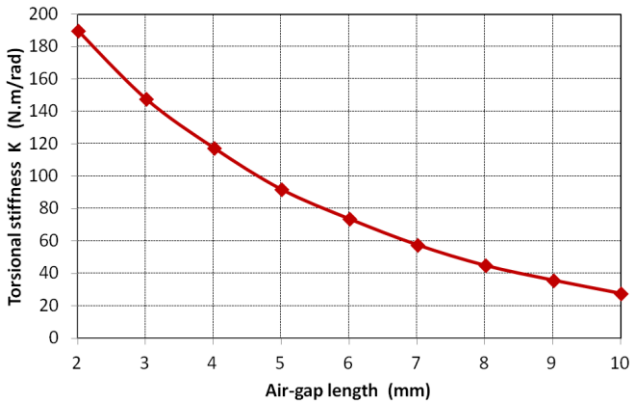

Fig. 6. *Torsional stiffness as a function of the air-gap length for δ_0 = 0°.*

$$T_c = T_{\max} \sin\left(2p(\theta_1 - \theta_2)\right) \qquad (2)$$

In order to obtain the torsional stiffness expression defined in (1), we have to make a linear approximation of (2) at a given operating load angle $\delta = \delta_0$ using the Taylor theorem. The torsional stiffness coefficient can then be written as follows

$$K = 2pT_{\max}\cos(2p\delta_0) \quad \text{with} \quad 0 < \delta_0 < \pi/4p \qquad (3)$$

It should be noted that the torsional stiffness depends directly on the pull-out torque and is a multiple of twice the number of pole pairs. Fig. 6 shows the torsional stiffness as a function of the air-gap length. It can be observed that the stiffness decreases when the air-gap increases, and reaches a value of around K = 60 N.m/rad for b = 7mm, which is much lower than the stiffness of mechanical couplings and can be the cause of large torsional oscillation between the two rotors during the transients, as will be seen later in the paper

3.2. Viscous Damping Coefficient

The viscous damping coefficient B is much more difficult to determine because 3D FE simulations must be performed by considering transient electromagnetic modeling with motion to predict the induced current in the

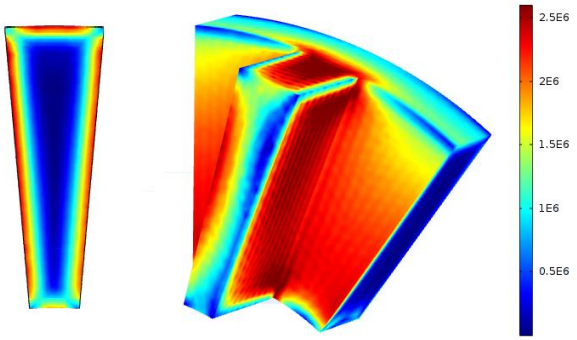

Fig. 7. *Eddy current distribution (module) in the salient-pole for a relative speed of 10 rad/s between the two rotors.*

salient pole due to the relative velocity between the two rotors. The simulations have been conducted using the *Rotating Machinery, Magnetic* interface in COMSOL Multiphysics.

Fig. 7 shows the eddy current distribution in a salient-pole at a given time and for a relative speed of 10 rad/s between the two rotors. It can be observed that induced currents are mainly distributed on the edge of the teeth due to the skin effect. It needs a fine mesh to converge towards the solution. The simulation times takes about 10 hours to obtain the result given in Fig. 7. From the knowledge of the current density distribution in steady-state condition, the eddy-current losses in salient-poles and back-iron is computed as follows

$$P_{eddy} = \frac{1}{\sigma}\int_{vol} J^2(x,y,z)dV \tag{4}$$

where J is the current density, V is the volume, and σ is the iron conductivity given in table 1.

Fig. 8 shows the average eddy-current losses as a function of the relative speed between the two rotors for three values of the air-gap. It can be seen that for the considered velocities, the eddy-current losses can be approximated as being proportional to the square of the relative speed and can then be written as follows

$$P_{eddy} = B\left(\Omega_1 - \Omega_2\right)^2 \tag{5}$$

where B is the damping coefficient to be determine.

From the eddy-current losses given in Fig. 8, we obtain the damping coefficient as a function of the air-gap length as shown in Fig. 9. As expected, the damping coefficient decreases with the air-gap and reaches a value of around B = 0.01 N.m/(rad/s) for b = 7mm.

4. Equations of Motion

4.1. Nonlinear Model

The governing equations of motion for the mechanical system of Fig. 3 are derived from Newton's second law for rigid body. If we consider a nonlinear spring

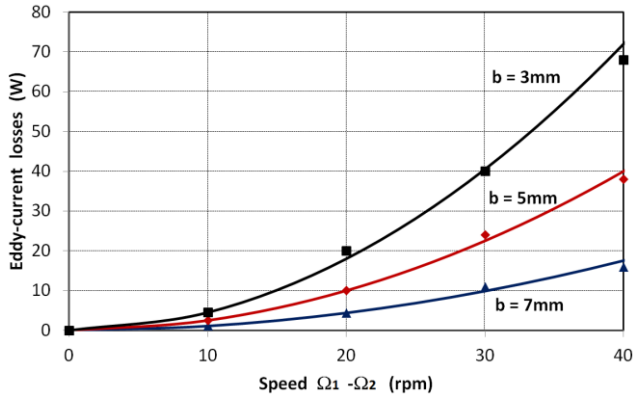

Fig. 8. *Eddy-current losses in the salient-pole versus the relative speed.*

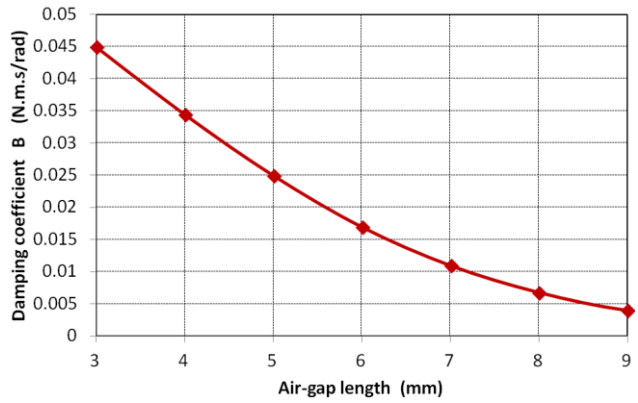

Fig. 9. *Damping coefficient as a function of the air-gap length.*

element for the magnetic coupling as defined in (2), the mathematical model consists of two coupled nonlinear differential equations for the angular shafts position θ_1 and θ_2

$$\begin{aligned} J_1\frac{d^2\theta_1}{dt} + B_1\frac{d\theta_1}{dt} &= T_1 - T_c \\ J_2\frac{d^2\theta_2}{dt} + B_2\frac{d\theta_2}{dt} &= T_c - T_2 \end{aligned} \tag{6}$$

with

$$T_c = T_{\max}\sin\left(2p\left(\theta_1-\theta_2\right)\right) + B\left(\frac{d\theta_1}{dt} - \frac{d\theta_2}{dt}\right) \tag{7}$$

The nonlinear model described by equations (6) and (7) will be simulated in the MATLAB/Simulink environment. The Simulink scheme is shown in Fig. 10.

4.2. Linearised Model

If we consider the linearised model for the spring stiffness as defined in (1), we obtain the following coupled linear differential equations for θ_1 and θ_2

$$\begin{aligned} J_1\frac{d^2\theta_1}{dt} + \left(B_1+B\right)\frac{d\theta_1}{dt} + K\theta_1 &= T_1 + K\theta_2 + B\frac{d\theta_2}{dt} \\ J_2\frac{d^2\theta_2}{dt} + \left(B_2+B\right)\frac{d\theta_2}{dt} + K\theta_2 &= K\theta_1 + B\frac{d\theta_1}{dt} - T_2 \end{aligned} \tag{8}$$

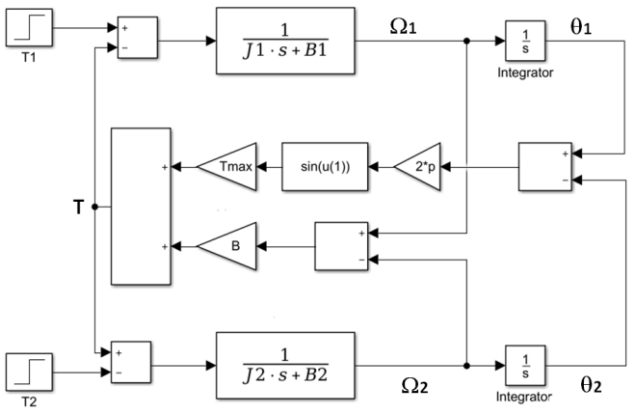

Fig. 10. *Simulink block-scheme for the nonlinear model.*

From these linear equations, it is possible to identify the damping factor and the oscillation period of both rotors, as discussed later in the document. In addition, most control design techniques are based on a linear model of the controlled system. Equations (8) can therefore be used to define a transfer function between the drive torque and the load rotor position, but this will not be developed here.

5. Experimental Results

For the experimental validation, we have manufactured an axial-flux reluctance coupler prototype. The prototype, which is placed between two electric motors, is shown in Fig. 2. The geometrical parameters of the prototype are given in Table 1. These geometrical parameters have been obtained after an optimization procedure but this is not within the scope of this paper. The optimization goals were to obtain a pull-out torque of 15 N.m for an air-gap length of 3 mm for a external radius set at R_2 = 60 mm and the minimum volume for the magnets.

The layout of the test bench is shown in Fig. 11 where the reluctance coupler is placed between two dc machines. One of the machines is used as a motor to impose the drive torque T_1 (main motor). It is powered by a dc chopper to control the armature current with a PI controller. A dc generator (secondary motor) is used to apply a sudden load torque by connecting a resistance to its terminals armature winding. Two high-resolution encoders (4096 pulses/revolution) are placed on the test bench to measure the relative angular position between the two rotors and to measure the speed on both sides of the coupling during the transient. The rotor of the dc generator can be locked if necessary. A photograph of the setup is given in Fig. 12.

The parameters of the drive system under consideration are given in Table 2. These parameters have been obtained by classical tests. The armature resistance R_a and the armature inductance L_a of the dc motor (main motor of Fig. 12) have been identified by the time response of the armature current to a step change in voltage (5V) as shown in Fig. 13. For this test, the rotor was locked.

The friction coefficients B_1 and B_2 were obtained from the no-load test for each dc motor. The motor's moment of inertia J_1 (the same for J_2) was measured from the velocity decay rate once current to the dc motor has been cut. For these tests, the two motors were mechanical decoupled, each with a part of the magnetic coupling.

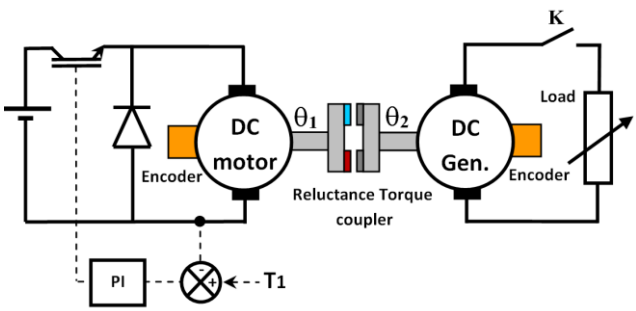

Fig. 11. *Test bench arrangement for the transient performance measurement.*

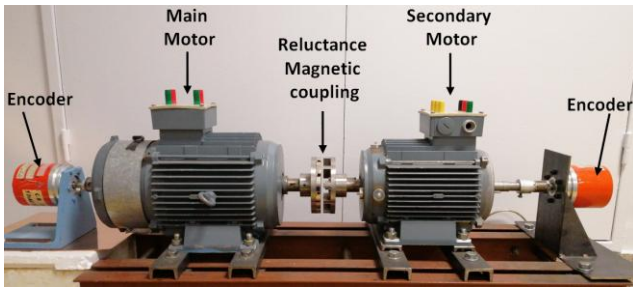

Fig. 12. *Experimental setup*

Table 2: Test bench parameters

Symbol	Quantity	value
J_1	Moment of inertia of the drive motor	0.025 kg.m^2
J_2	Moment of inertia of the load	0.013 kg.m^2
B_1	Friction coefficient of the drive motor	2e-3 Nm/rd/s
B_2	Friction coefficient of the load	2e-3 Nm/rd/s
R_a	Armature resistance of the dc motor	2.5 Ω
L_a	Armature inductance of the dc motor	0.02 H
K_T	Torque constant of the dc motor	1.35 Nm/A

The torsional stiffness and the damping coefficient for the reluctance coupler are given in Fig. 6 and Fig. 9, respectively.

In the following sections, we study two types of transient responses and we compare the simulation results with tests. For the simulation results, we will consider the model with or without damping effect to highlight the differences.

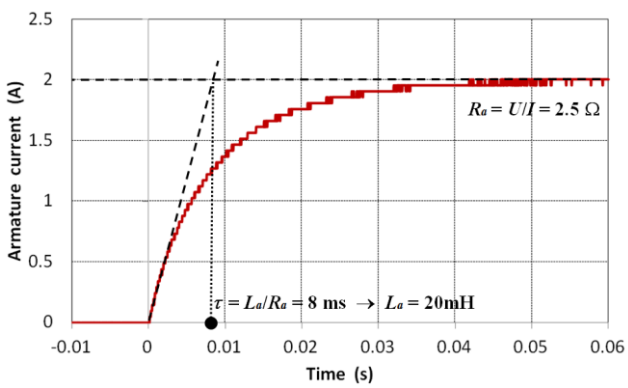

Fig. 13. *Time response of the armature current to a step change in voltage (U = 5V).*

5.1. Rotor Position Response to a Step Input on the Drive Torque T_1

The first test concerns the angular rotor position response to a step input in the drive torque T_1 when the other side of the magnetic coupling is locked (θ_2 = 0°). As explained previously, the control of the drive torque is done by regulating the armature current of the dc motor.

The experimental results are given in Figs. 14. As shown in fig. 14(a), the dc motor applies a torque which is zero for t < 0s and increases to a step of 4 N.m at t = 0s. The transient responses for three values of the rotor position are given in Fig. 14(b). We can see large oscillations in the rotor position during the transient. The oscillation period T increases with the air-gap value. This is due to the decrease of the torsional stiffness as shown in Fig. 6.

As the tests were performed for small variation in the rotor position, we can use the linearised model defined in (8) to analyze the results obtained in Figs. 14. From (8) and considering θ_2 = 0, we obtain the following second-order differential equation between the rotor position and the drive torque.

$$J_1 \frac{d^2\theta_1}{dt} + (B_1 + B)\frac{d\theta_1}{dt} + K\theta_1 = T_1 \qquad (9)$$

If we consider an under-damped system that corresponds to the experimental results of Fig. 14(b), the damping ratio ζ and the natural frequency ω_n are given by:

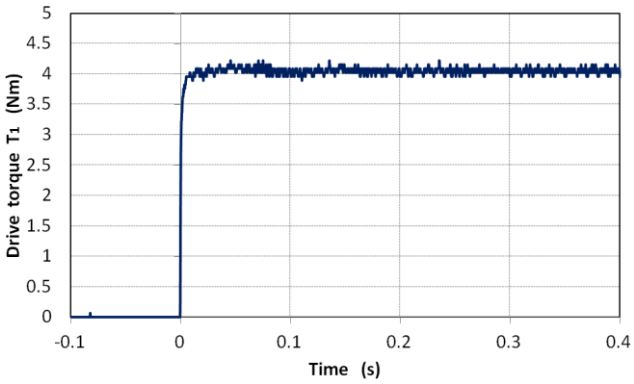

(a)

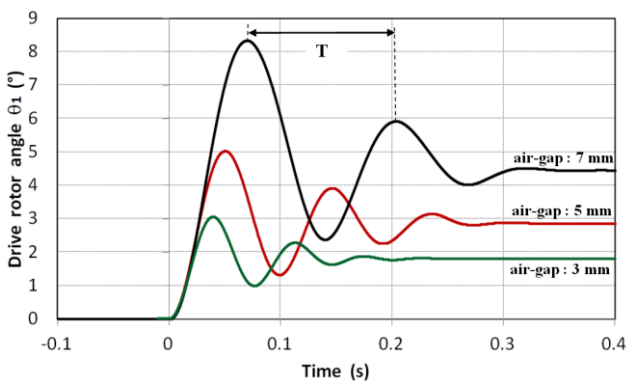

(b)

Fig. 14. *Transient responses to a step input in the drive torque, (a) Drive torque T_1, (b) Rotor position for b = 3 mm, b = 5 mm, and b = 7 mm, Experimental results.*

Table 3: Comparison between the model and the test for the oscillation period

		airgap b = 3 mm	airgap b = 5 mm	airgap b = 7 mm
K (N.m/rad)		150	90	60
B (N.m.s/rad)		0.045	0.025	0.011
T (ms)	Model	**73**	**94**	**115**
	Experimental	**75**	**96**	**126**

$$\xi = \frac{B_1 + B}{2\sqrt{KJ_1}} \qquad \omega_n = \sqrt{\frac{K}{J_1}} \qquad (10)$$

From (10), we obtain the classical expression for the oscillation period for a second-order system

$$T = \frac{2\pi}{\omega_n\sqrt{1-\xi^2}} \qquad (11)$$

In order to show the accuracy of the proposed model, Table 3 compares the oscillation period T for simulation and tests. In all cases, the error is less than 10%.

5.2. Transient Performance During Start-Up

For the second test, we study the transient performance during start-up by considering two values for the air gap length: 5 mm and 7 mm. The results are given in Fig. 15 and Fig. 16, respectively.

The transient performances are evaluated by running the dc motor from the stop (at t = 0 s) at a speed of 400 rpm under no load condition. A step voltage U_{dc} = 58 V is applied to the dc motor at t = 0 s. Because these tests correspond to large variations in the rotors positions, the simulations were performed using the non-linear model of Fig. 10, adding the dc motor model whose parameters are given in Table 2.

The results obtained for b = 5 mm are given in Fig. 15. It can be observed speed oscillations between the two rotors before the synchronization. This is due to the low stiffness specific to synchronous magnetic couplings [12]. The simulation result presented in Fig. 15 (dotted line) shows a fairly good agreement with the test. The difference between test and simulation can be explained by the armature inductance variation caused by the magnetic saturation due to the field current. The armature inductance was measured without the field current (Fig. 13). For an air-gap of 5 mm, one can observe that the speed of the two rotors remains close to each other during the starting. This is no longer the case if we consider a higher air-gap value, as shown in Fig. 16.

The test result given in Fig. 16(a) corresponds to an air-gap of 7 mm. It shows that for this large air-gap, the start-up is now a two-step process. At the beginning (t < 1.2 s), the speed difference between the two rotors is important.

For this stage, the torque transmitted through the magnetic coupling is mainly due to the damping effect (asynchronous torque). Then, synchronization between the two rotors occurs with large oscillations at $t \approx$ 1.2s. This is

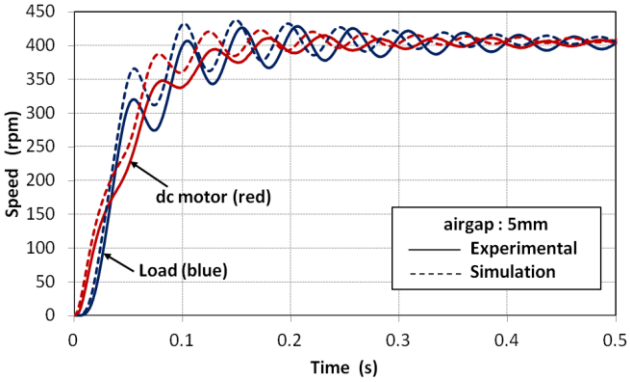

Fig. 15. *Start-up of the shaft line for an air-gap b = 5mm: (———) Experimental result, (------) Simulation.*

due to the synchronous torque between the magnets and the salient poles which becomes predominant. Finally, the two rotors pull into synchronism at around t = 2s. This result is very different from the one we had obtained for a synchronous magnetic coupling with permanent magnets placed on the 2 rotors [12]. This can be explained from the electrical conductivity of the salient-pole which is around ten times greater than the electrical conductivity of the NdFeB magnets and causes a significant asynchronous torque at start-up.

As shown in Fig. 16(b), the transient behaviour of the shaft-line during start-up is well predicted if the damping effect is taken into account in the simulation. This is no longer the case if we consider the magnetic coupling without damper (B = 0), as can be seen in Fig. 16(c) where the synchronism between the two rotors is lost at the beginning of the start, that does not correspond to the test. This last result clearly shows that it is necessary to represent the reluctance magnetic coupling by the equivalent mechanical model illustrated in Fig. 3, with the two components: spring and damper. It can be noted that the transient behaviour of a reluctance magnetic coupling during the start-up with asynchronous and synchronous torque is similar to that of a line start synchronous reluctance machine with a damper cage winding, although the analytical models for their study are not the same [22-23].

It is worth noting that oscillations between the two rotors during starting (as shown in Fig. 15) can be problematic to achieve high performance for speed or position control in servomechanism applications [24]. If a reluctance magnetic coupling is used to transmit the torque between two shafts, its transfer function with damping and stiffness coefficients (8) must be taken into account when designing the PID controller.

6. Conclusion

In this paper, we have developed a new tool to effectively predict the transient characteristics of a shaft line including a reluctance magnetic coupling. We have shown that the reluctance coupler causes speed oscillations between the two shafts when starting. One of the most important contributions of this paper is the consideration of the damping effect due to the induced currents in the salient poles during the transient which cannot be neglected in order to obtain good predictions. This damping effect is

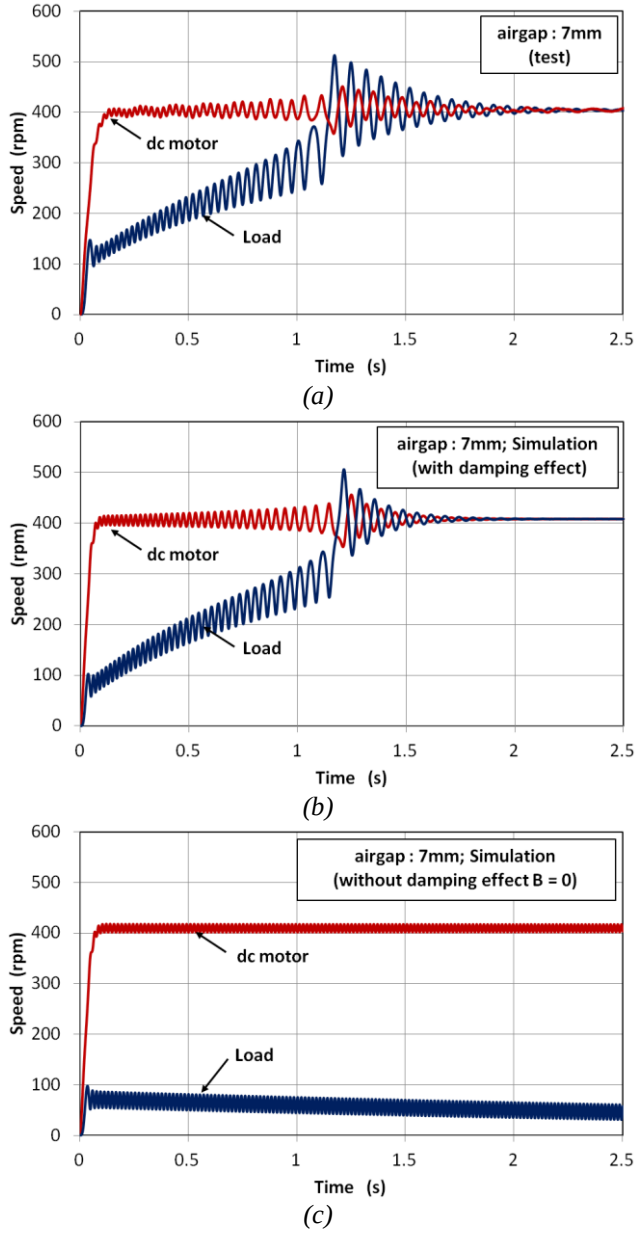

Fig. 16. *Start-up of the shaft line for an air-gap b = 7mm: (a) experimental result, (b) simulation with damping effect, (c) simulation without damping effect..*

advantageous because it prevents the stall between the two shafts when starting. Comparisons between experimental and simulation results have clearly demonstrated the value of the proposed model.

7. References

[1] Furlani E. P., 'Analysis and optimization of synchronous couplings', 1996, *J. Appl. Phys.*, **79**, pp. 4692–4694.

[2] Waring R., Hall J., Pullen K., Etemad M. R., 'An investigation of face type magnetic couplers', 1996, *Proc. Inst. Mech. Engrs*, **210**, (4), pp. 263–272.

[3] Choi J. Y., Shin H. J., Jang S. M., Lee S. H., 'Torque analysis and measurements of cylindrical air-gap synchronous permanent magnet couplings based on analytical magnetic field calculations', 2013, *IEEE Trans. Magn.*, **49**, (7), pp. 3921-3924.

[4] Mohammadi S., Mirsalim M., Vaez-Zadeh S., Talebi H. A., 'Analytical modeling and analysis of axial-flux interior permanent-magnet couplers', *IEEE Trans. Ind. Electron.*, 2014, **61**, (11), pp.5940 -5947.

[5] Dolisy B., Mezani S., Lubin T., Lévêque J., 'A new analytical torque formula for axial field permanent magnets coupling', 2015, *IEEE Trans. Energy Convers*., **30**, (3), pp. 892-899.

[6] Mohammadi S., Mirsalim M., Vaez-Zadeh S., 'Non-linear modeling of eddy-current couplers', *IEEE Trans. Energy Convers.*, 2014, **29**, (1), pp. 224–231.

[7] Mouton Z., Kamper M. J., 'Modeling and optimal design of an eddy current coupling for slip-synchronous permanent magnet wind generators', *IEEE Trans. Ind. Electron.*, 2014, **61**, (7), pp. 3367–3376.

[8] Wang J., Lin H., Fang S., 'Analytical Prediction of Torque Characteristics of Eddy Current Couplings Having a Quasi-Halbach Magnet Structure', 2016, *IEEE Trans. Magn.*, **52**, (6), 8001209.

[9] Mohammadi S., Mirsalim M., 'Double-Sided permanent-magnet radial-flux eddy-current couplers: three-dimensional analytical modeling, static and transient study, and sensitivity analysis', *IET Electr. Power Appl.*, 2013, **7**, (9), pp. 665–679.

[10] Nagrial M. H., 'Analysis and performance of variable reluctance (V. R.) torque coupler', *Proc. IEEE Conference on Industrial Automation and Control Emerging Technology Applications*, May 1995, pp. 136-139.

[11] Nagrial M. H., 'Finite element analysis and design of variable reluctance (VR) torque couplers', *Proc. International conference on power electronics and drive systems*, May 1997, pp. 252-254.

[12] Lubin T., Mezani S., Rezzoug A., 'Experimental and theoretical analyses of axial magnetic coupling under steady-state and transient operation', *IEEE Trans. Ind. Electron.*, 2014, **61**, (8), pp. 4356-4365.

[13] Lubin T., Rezzoug A., 'Steady-state and transient performance of axial-field eddy-current coupling, *IEEE Trans. Ind. Electron.*, 2015, **62**, (4), pp. 2287–2296.

[14] Lubin T., Fontchastagner J., Mezani S., Rezzoug A., 'Comparison of transient performances for synchronous and eddy-current torque couplers', *XXII. International conference on Electrical Machines*, Sept. 2016, pp. 695-701.

[15] Wu W., Lovatt H. C., Dunlop J. C., 'Analysis and design optimisation of magnetic couplings using 3D finite element modelling', *IEEE Trans. Magn.*, 1997, **33**, (5), pp. 4083–4085.

[16] Chan T. F., Wang W., Lai L. L., 'Performance of an Axial-Flux Permanent Magnet Synchronous Generator From 3-D Finite-Element Analysis', 2010, *IEEE Trans. Energy. Convers.*, 25, (3), pp. 669-676.

[17] Desvaux M., Le Goff Latimier R., Multon B., Sire S., Ben Ahmed H., 'Analysis of the dynamic behaviour of magnetic gear with nonlinear modelling for large wind turbines', *Proc. XXII International Conference on Electrical Machines* (*ICEM*), Sept 2016, pp. 1332-1338.

[18] Liu X., Zhao Y., Zhang X., Gao J., Huang S., 'Investigation of the dynamic characteristics of a coaxial magnetic gear under loading condition based on analytical model ', *20th International Conference on Electrical Machines and Systems (ICEMS)*, Aug 2017, pp. 1-5.

[19] Davis E. J., Wright M. T., Jonhson R. C., "Transient performance of eddy-current couplings," *Proc. IEE*, 1975, **122**, (10), pp. 1128-1136.

[20] Amati N., Tonoli A., Canova A., Padovani M., 'Dynamic behaviour of torsional eddy-current dampers: sensitivity of the design parameters', *IEEE Trans. Magn.*, 2007, **43**, (7), pp. 3266–3277.

[21] Aberoomand V., Mirsalim M., Fesharakifard R., 'Design optimization of double-sided permanent-magnet axial eddy-current couplers for use in dynamic applications, 2019, *IEEE Trans. Energy Convers*., **34**, (2), pp. 909-920.

[22] Ogunjuyigbe A. S. O., Jimoh A. A., Ayodele T. R., 'Dynamic and transient behavior of a line start, capacitance compensated synchronous reluctance machine', *Journal of Electrical Systems and Information Technology.*, 2018, **7**, pp. 843–860.

[23] Mingardi D., Bianchi N., 'Line-start PM-assisted synchronous motor design, optimization, and tests', *IEEE Trans. Ind. Electron.*, 2017, **64**, (12), pp. 9739-9747.

[24] Montague R. G., Bingham C. M., Atallah K., 'Characterisation and modelling of magnetic couplings and gears for servo control systems', *IET 5th International Conference on Power Electronics, Machines & Drives* (*PEMD*), Apr 2010, pp. 1-6.